

Article

Organic Matter Enrichment Mechanisms in the Lower Cambrian Shale: A Case Study from Xiangandi #1 Well

Lei Zhou^{1,2,3}, Xingqiang Feng^{1,2,3,*}, Linyan Zhang^{1,2,3} and Lin Wu^{1,2,3}

¹ Institute of Geomechanics, Chinese Academy of Geological Sciences, Beijing 100081, China; zhoulei4010@126.com (L.Z.); zhanglinyan2015@163.com (L.Z.); wulin50@mail.cgs.gov.cn (L.W.)

² Key Laboratory of Petroleum Geomechanics, Chinese Academy of Geological Sciences, Beijing 100081, China

³ Key Laboratory of Paleomagnetism and Tectonic Reconstruction of Ministry of Natural Resources, Chinese Academy of Geological Sciences, Beijing 100081, China

* Correspondence: fxingqiang@mail.cgs.gov.cn

Abstract: In order to investigate the effect of primary productivity, organic matter dilution, and preservation on the accumulation of organic matter, geochemical data, and proxies of primary productivity, clastic influx, and redox conditions were obtained for organic-rich shales in the Cambrian Niutitang Formation. The primary productivity (total organic carbon [TOC], Mo, P, Ba, and Babiio) and redox (Ni/Co, V/Cr, U/Al, and Th/U) proxies suggest the organic-rich shales were deposited in anoxic-euxinic conditions during periods of high primary productivity. Pyrite in the Niutitang Formation comprises spherical framboids, which also indicate that anoxic bottom waters were present during organic matter deposition. High primary productivity enhanced the organic C flux into the thermocline layer and bottom waters, which lead to the development of anoxic bottom waters owing to O₂ consumption by microorganisms and organic matter degradation. The anoxic bottom waters were beneficial for the preservation of organic matter. In addition, Ti/Al ratios correlate well with TOC contents throughout the Niutitang Formation, indicating that clastic input increased the burial rate and prevented organic matter degradation during deposition. Therefore, the accumulation of organic matter in the Niutitang Formation was controlled mainly by primary productivity rather than bottom-water redox conditions.

Keywords: primary productivity; dilution; preservation; organic matter; accumulation



Citation: Zhou, L.; Feng, X.; Zhang, L.; Wu, L. Organic Matter Enrichment Mechanisms in the Lower Cambrian Shale: A Case Study from Xiangandi #1 Well. *Minerals* **2024**, *14*, 183. <https://doi.org/10.3390/min14020183>

Academic Editors: Rui Yang, Zhiye Gao, Yuguang Hou and Santanu Banerjee

Received: 6 December 2023

Revised: 24 December 2023

Accepted: 27 December 2023

Published: 8 February 2024



Copyright: © 2023 by the authors. Licensee MDPI, Basel, Switzerland. This article is an open access article distributed under the terms and conditions of the Creative Commons Attribution (CC BY) license (<https://creativecommons.org/licenses/by/4.0/>).

1. Introduction

Variations of organic matter accumulation in sediments are relatively large, as a result of a complex interaction between productivity, preservation, and dilution of organic matter [1–3]. The primary productivity associated with different nutrient and organic matter types can provide important insights into the organic matter in shales and mudstones [4–7]. Dilution of organic matter is a complex function of sedimentation rates [8,9] and biogenic alteration of inorganic matter [2,10]. The redox conditions of seawater also have a significant effect on the preservation of organic matter and can prevent its oxidation and destruction in sediments [11–15]. Organic matter enrichment in shales has been explained by two distinct models, i.e., the primary productivity and preservation models [5–12].

The Lower Cambrian Niutitang Formation in the Middle and Upper Yangtze regions consists mainly of bedded siliceous shale, laminated shale, muddy siltstone, and sandstone [16]. The third-order sequence of the Niutitang Formation is a transgressive systems tract (TST), consisting mainly of siliceous and calcareous shales, and a highstand systems tract (HST), consisting mainly of argillaceous and silty mixed shales. The absence of a lowstand systems tract (LST) can be attributed to rapid transgression at the Ediacaran–Cambrian boundary [17,18]. Organic matter contents vary in the different sedimentary facies and decrease from the deep-water shelf to the shallow-water shelf and

tidal flat facies [19]. Owing to negligible fractionation during sediment transport and deposition, geochemical data and proxies obtained from the clastic sediments provide important insights into their palaeoenvironments during deposition [20–23]. Shields and Stille discussed the effects of post-depositional diagenesis on rare earth elements (REEs) in the basal Cambrian phosphorites of the Meishucun section [24]. Li et al. and Zhou et al. proposed that seawater made a greater contribution to REE contents than hydrothermal inputs in the Niutitang Formation phosphatic, siliceous, and silty mixed shales [25,26]. Several studies have investigated the geochronology and geochemistry of the Niutitang Formation and the processes responsible for organic matter enrichment [27–30]. However, few studies have investigated the effects of primary productivity and organic matter dilution on organic matter accumulation. In this study, the geochemical compositions of the Niutitang Formation shales were used to determine variations in primary productivity, organic matter dilution and preservation in order to develop a better understanding of organic matter accumulation in organic-rich shales.

2. Samples and Method

The Xiangandi #1 well (XAD 1 well) is located near Anhua, in central Hunan Province (Figure 1). The Niutitang Formation overlies the chert successions of the Liuchapo Formation and contains mainly black organic-rich shales intercalated with gray limestones. The 53 samples from the Niutitang Formation and 2 samples from the Liuchapo Formation were selected from XAD 1 well for major and trace elements analysis (Figure 1c).

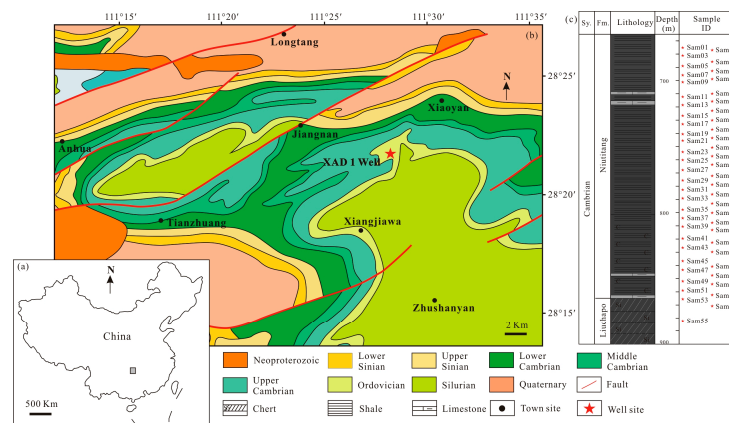


Figure 1. Simplified geological map in the southeast Yangtze Platform margin and lithological profile of XAD 1 well section. (a) Location map of the studied area in China, (b) Simplified geological map of Anhua County, Hunan Province, (c) lithological profile and sample sites of XAD 1 well.

Argon ion polished thin sections, taken perpendicular to the bedding orientation, were observed using a Quanta FEG 450 scanning electron microscope. The micrographs were employed to study the morphology of the minerals. Total organic carbon (TOC) content was determined using the carbon/sulfur analyzer. Major element concentrations of SiO_2 , Al_2O_3 , CaO , TFe_2O_3 , K_2O , MgO , MnO , Na_2O , P_2O_5 , and TiO_2 were determined using an AxiosmAX X-ray fluorescence spectrometer following experimental details of Li et al. [25]. The relative precision of major-element concentrations in the Lower Cambrian Niutitang Formation shales was $<\pm 5\%$. The trace elements concentrations of Mo, Ba, Cu, Ni, Co, V, Cr, and U were determined using an ELEMENT XR plasma mass spectrometer (National Research Center for Geoanalysis, Chinese Academy of Geological Sciences, Beijing, China) following experimental details of Zhou et al. [26], with a relative precision of $<\pm 5\%$. Element enrichment factors (EF_{element}) were defined as follows: $EF_{\text{element}} = (\text{element}/\text{Al})_{\text{sample}} / (\text{element}/\text{Al})_{\text{average shale}}$, where $(\text{element}/\text{Al})_{\text{average shale}}$ refers to the data from an average shale [31]. The major elements concentrations, trace elements concentrations, and TOC content of the Niutitang Formation shales are presented in Tables 1 and 2.

Table 1. The major element concentrations (%) of the Niutitang Formation shales.

Samples ID	Depth/m	SiO ₂	Al ₂ O ₃	TFe ₂ O ₃	MgO	CaO	Na ₂ O	K ₂ O	MnO	TiO ₂	P ₂ O ₅
Sam.01	675.3	61.95	8.08	9.72	2.26	3.70	0.46	2.69	0.02	0.39	0.052
Sam.02	677.1	68.53	11.35	3.43	2.01	1.30	0.68	3.96	0.01	0.59	0.066
Sam.03	681.2	74.41	7.91	3.44	2.32	1.40	0.57	2.56	0.01	0.38	0.051
Sam.04	686	76.14	8.55	3.03	1.48	0.56	0.39	2.95	<0.01	0.42	0.068
Sam.05	689	66.97	11.28	4.66	1.55	2.41	0.60	3.86	0.02	0.54	0.094
Sam.06	692.8	71.89	9.58	3.97	1.41	0.81	0.39	3.33	<0.01	0.47	0.062
Sam.07	695.9	67.60	7.72	2.93	2.47	4.68	0.07	2.63	0.01	0.40	0.07
Sam.08	698.9	73.76	8.62	3.73	1.21	0.16	0.05	2.89	<0.01	0.44	0.056
Sam.09	701.2	63.12	13.69	5.54	2.52	0.36	0.07	4.33	0.01	0.71	0.10
Sam.10	709.8	5.41	0.47	0.73	3.02	48.34	0.13	0.07	0.03	0.03	0.036
Sam.11	712.3	73.09	10.71	3.69	1.41	0.16	0.62	3.06	<0.01	0.47	0.074
Sam.12	715.6	6.32	0.79	1.15	2.61	47.57	0.16	0.09	0.04	0.04	0.044
Sam.13	718.5	5.62	0.72	0.81	2.49	48.52	<0.05	0.10	0.03	0.04	0.035
Sam.14	722.8	78.31	6.62	2.30	1.09	2.09	0.14	1.97	<0.01	0.31	0.06
Sam.15	726.6	66.4	5.78	6.09	4.72	4.58	0.06	0.95	0.03	0.22	0.082
Sam.16	729.6	70.62	11.5	3.72	1.59	0.72	0.06	3.52	<0.01	0.37	0.063
Sam.17	732.9	54.49	9.74	5.98	9.18	5.35	0.06	1.47	0.06	0.39	0.071
Sam.18	737	72.04	9.79	3.16	1.24	0.89	0.11	2.89	0.02	0.35	0.093
Sam.19	740.5	72.22	9.44	4	1	0.27	0.18	2.73	<0.01	0.36	0.074
Sam.20	743.4	73.37	9.87	2.96	1.17	0.43	0.11	2.97	<0.01	0.38	0.069
Sam.21	745.4	71.32	9.29	4.42	1.06	1.62	0.36	2.9	0.02	0.38	0.073
Sam.22	750.6	69.3	11.15	4.13	1.37	1.45	0.13	3.32	0.02	0.46	0.082
Sam.23	754.1	59.14	10.72	5.7	1.28	6.75	0.38	3.02	0.05	0.39	0.081
Sam.24	757.2	73.91	10.43	2.79	1.14	0.41	0.16	3.04	<0.01	0.39	0.057
Sam.25	760	74.79	10.4	2.84	1.26	0.8	0.08	3.12	0.02	0.35	0.079
Sam.26	763.6	71.44	11.41	3.11	1.29	0.36	0.2	3.25	0.01	0.33	0.086
Sam.27	767.6	67.11	10.54	5.26	1.32	1.34	0.18	3.14	0.02	0.38	0.105
Sam.28	772	65.66	11.35	5.32	2.38	2.62	0.11	3.29	0.04	0.37	0.101
Sam.29	775.6	74.79	8.22	3.01	1.21	0.59	0.06	2.44	0.01	0.34	0.102
Sam.30	778.6	78.73	7.04	2.01	0.89	0.83	0.07	2.04	0.02	0.29	0.094
Sam.31	782.4	78.2	5.85	2.6	1.25	0.45	<0.05	1.62	<0.01	0.29	0.061
Sam.32	786.4	64.42	10.71	4.53	1.99	0.88	0.05	2.85	0.02	0.54	0.148
Sam.33	789.3	72.4	4.67	2.13	1.44	4.26	<0.05	1.06	0.03	0.22	0.158
Sam.34	793.4	73.4	5.82	3.71	1.33	0.8	<0.05	1.55	0.01	0.29	0.108
Sam.35	797.6	78.1	5.08	2.66	0.77	0.72	<0.05	1.41	<0.01	0.2	0.147
Sam.36	800	59.9	8.01	4.89	1.26	0.29	<0.05	2.17	<0.01	0.35	0.153
Sam.37	804	58.86	5.84	4.53	2.64	0.73	0.08	1.7	0.01	0.34	0.466
Sam.38	807.8	64.98	6.59	4.86	0.63	0.71	0.23	2.11	<0.01	0.35	0.297
Sam.39	810.5	62.29	7.03	4.22	1.63	1.44	0.34	2.13	0.01	0.42	0.221
Sam.40	813.3	77.56	2.94	1.15	1.16	2.18	0.18	0.74	0.01	0.14	0.076
Sam.41	819.35	69.74	5.06	1.75	1.87	0.98	0.1	1.26	0.01	0.27	0.15
Sam.42	822.6	83.66	2.38	1.04	0.35	0.34	0.1	0.65	<0.01	0.11	0.166
Sam.43	826.5	71.41	6.98	2.25	0.94	1.02	0.21	2.07	0.01	0.38	0.316
Sam.44	829.7	79.77	2.69	1.18	0.83	1.84	0.06	0.72	0.01	0.14	0.138
Sam.45	836.8	62.84	7.11	4.79	1.05	1.01	0.07	2.12	<0.01	0.37	0.563
Sam.46	840.6	76.59	1.59	0.91	0.78	2.15	<0.05	0.29	0.01	0.07	0.344
Sam.47	843.4	65.94	7.29	3.61	0.74	0.74	0.07	2.04	<0.01	0.39	0.30
Sam.48	847.5	35.34	4.99	3.36	16.93	16.36	<0.05	0.76	0.08	0.21	0.10
Sam.49	852	94.12	0.8	0.44	0.08	0.85	<0.05	0.05	<0.01	0.01	0.25
Sam.50	854.3	84.89	0.89	0.9	0.5	4.38	<0.05	0.16	<0.01	0.06	0.082
Sam.51	859	74.56	4.3	2.25	1.23	1.13	<0.05	1.42	<0.01	0.19	0.174
Sam.52	862.5	25.24	0.9	0.18	2.65	30.03	<0.05	0.17	0.04	0.02	0.445
Sam.53	865.5	79.01	4.77	2.82	2.67	3.1	0.16	1.46	0.03	0.27	0.035
Sam.54	870.8	76.08	9.32	3.82	2.06	0.38	<0.05	2.96	<0.01	0.54	0.022
Sam.55	882.3	98.82	0.37	0.3	0.08	0.1	<0.05	0.13	<0.01	0.02	0.012

Table 2. The trace element concentrations (ppm) and TOC contents (%) of the investigated shales.

Samples ID	Depth/m	TOC	Mo	Ba	Cu	Ni	Co	V	Cr	U	Th
Sam.01	675.3	6.57	35.8	1033	117	80	17.1	110	74.8	10.4	9.27
Sam.02	677.1	4.85	49.5	1257	64.1	79.7	16.3	182	84.9	9.1	13.5
Sam.03	681.2	4.33	29.4	1031	49.3	48	14.3	86.8	67.8	11.5	9.89
Sam.04	686	4.42	30.5	1166	52.8	49.2	13.9	92.6	76.5	14.2	10.6
Sam.05	689	4.39	36.4	1394	73.4	53	20.4	100	77.3	11.7	12.4
Sam.06	692.8	6.1	87.8	1307	98	81.3	16.5	178	72.4	19.7	11.2
Sam.07	695.9	4.52	45.5	979	73.9	75	10.9	157	82.6	10.5	8.69
Sam.08	698.9	5.68	80.2	919	116	73.8	18	121	77.2	19.4	10.8
Sam.09	701.2	6.58	57.9	1081	96.4	54.2	22.4	129	95.1	19.5	14.9
Sam.10	709.8	0.48	0.44	175	2.6	9.08	1.3	5.71	8.05	0.58	0.56
Sam.11	712.3	4.28	48.8	1266	106	79.1	15.8	133	74.1	14	11.2
Sam.12	715.6	0.84	2.27	175	8.97	9.02	1.95	12.5	10.4	1.3	0.82
Sam.13	718.5	0.69	0.65	213	3.55	8.5	1.66	11.1	7.84	1.15	0.65
Sam.14	722.8	3.54	32.3	843	113	74.4	9.97	186	86.9	9.49	7.34
Sam.15	726.6	5.41	5.1	390	72.4	26.2	8.24	61.9	86.2	9.79	5.43
Sam.16	729.6	4.06	33.9	1407	72.8	90.6	16.2	221	71	9.38	12
Sam.17	732.9	4.64	19.8	662	66.7	40.8	17.2	78.5	78.4	7.64	10.7
Sam.18	737	5.43	40	1333	71.6	53.5	14.3	95.6	75.4	10.2	10.8
Sam.19	740.5	6.01	28.4	1449	55.2	68.3	13.4	104	67.8	7.21	9.91
Sam.20	743.4	5.19	33	1547	70.8	43.4	13.6	82.8	66.7	7.76	10.1
Sam.21	745.4	5.79	30.6	1413	64.3	43.1	14.2	82.3	67.8	7.82	9.53
Sam.22	750.6	5.33	50.9	1633	81.4	58.3	17.5	119	75.6	11.9	11.3
Sam.23	754.1	6.22	49.8	1436	69.4	82.1	14.9	154	70.9	8.88	9.91
Sam.24	757.2	4.44	33.8	1737	56.4	95.3	13.5	391	71.5	9.01	9.92
Sam.25	760	4.18	26.4	1690	50.5	78.7	13.8	226	73.6	6.85	10.5
Sam.26	763.6	4.59	62.7	1987	65.9	123	15.3	571	87.9	11.9	10.3
Sam.27	767.6	7.48	63.5	1830	69.9	99.3	13.8	512	89.1	13.6	11.1
Sam.28	772	5.14	36.6	1685	84.7	122	17.5	344	98.4	11.3	9.53
Sam.29	775.6	6.78	69.1	1633	52	92.2	12.9	185	75	31.5	8.88
Sam.30	778.6	5.9	29.6	2121	35.9	58.4	9.64	150	62.2	15.9	6.56
Sam.31	782.4	6.1	49.7	1508	60	82.4	10.3	149	70.5	22.6	6.9
Sam.32	786.4	10.1	110	2524	108	88.5	19.1	253	88.4	54.9	12.5
Sam.33	789.3	8.63	88.4	1149	55.3	42.9	8.5	135	77.1	32.3	5.36
Sam.34	793.4	9.74	45.6	2278	88.5	65.5	17.2	161	59.7	35.9	7.05
Sam.35	797.6	8.4	107	2511	496	278	10.1	2479	617	18.3	4.96
Sam.36	800	18.24	270	3474	155	617	17.6	4500	480	59	7.5
Sam.37	804	19.89	437	11,801	74.2	493	17.6	1272	78.2	214	5.26
Sam.38	807.8	14.63	249	14,222	174	147	12.4	1635	127	79	4.81
Sam.39	810.5	12.61	185	17,789	56.2	181	11.8	1148	84.6	79.6	4.72
Sam.40	813.3	9.13	34.1	9041	30.3	66.3	3.71	130	102	87.5	2.22
Sam.41	819.35	9.92	91.9	15,631	1386	155	6.59	2538	172	38.6	2.92
Sam.42	822.6	10	32.6	7731	15.3	67.2	4.16	425	101	49.7	1.75
Sam.43	826.5	8.27	151	17,055	111	173	12.1	1841	193	56.4	4.68
Sam.44	829.7	9.25	98.9	9030	34.1	151	4.7	605	139	82.6	2.04
Sam.45	836.8	13.09	172	16,876	467	516	14.2	7585	517	40.9	5.01
Sam.46	840.6	12.92	22.8	8938	172	71.8	3.62	3483	182	19.3	1.11
Sam.47	843.4	12.42	154	40,781	125	227	13.3	3349	189	43.6	3.96
Sam.48	847.5	2.1	10.8	27,475	35.4	29.5	9.73	652	141	3.52	2.24
Sam.49	852	13.12	6.43	9941	268	29.2	0.92	1215	265	29.6	0.4
Sam.50	854.3	4.76	182	6632	169	51	3.23	1234	445	118	1.33
Sam.51	859	10.88	144	3584	93.4	94.9	14.6	6880	871	42.5	3.43
Sam.52	862.5	4.54	33.9	56,893	97.4	49.4	4.74	539	133	9.15	0.26
Sam.53	865.5	2.01	4.65	4331	16.1	15.1	3.4	58.4	175	1.97	5.5
Sam.54	870.8	4.05	0.98	2198	27	45.9	5.31	134	108	5.14	6.9
Sam.55	882.3	0.13	0.7	265	2.83	4.89	0.48	12.3	157	0.55	0.45

3. Results

3.1. TOC Content

TOC contents range from 2.01% to 19.8% (average = 7.62%) for the Niutitang Formation shales. TOC contents range from 0.13% to 4.05% (average = 2.09%) for the Liuchapo Formation sediments.

3.2. Major Element

SiO₂ contents vary from 54.49% to 94.12% (average = 71.33%) for the Niutitang formation shales, and from 76.08% to 98.82% (average = 87.45%) for the Liuchapo Formation sediments (Table 1). Al₂O₃ contents are 0.8%–13.69% (average = 7.65%) for the Niutitang Formation shales, and 0.37%–9.32% (average Al₂O₃ = 4.85%) for the Liuchapo Formation sediments. CaO contents vary from 0.16% to 6.75% (average = 1.6%) for the Niutitang Formation shales, and from 0.1% to 0.38% (average = 0.24%) for the Liuchapo Formation sediments. Enrichment factors of major elements indicate that SiO₂, ¹Fe₂O₃, CaO, and P₂O₅ are enriched in the Niutitang Formation shales, whereas MgO, Na₂O, K₂O, MnO, and TiO₂ are not markedly enriched (Figure 2).

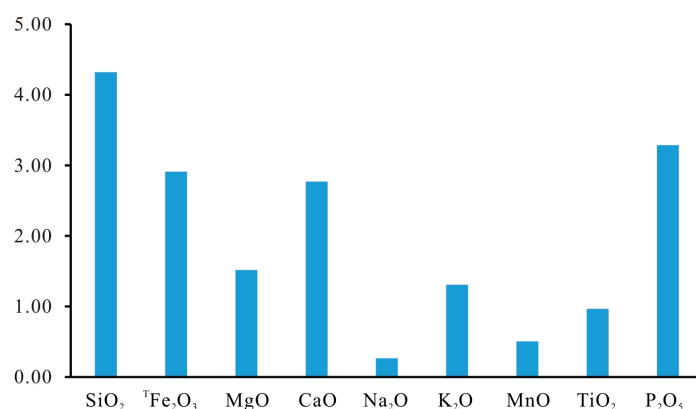


Figure 2. Enrichment factors (EF) of major elements in the Niutitang Formation shales relative to average shale.

3.3. Trace Element

Concentrations of Mo, Ba, Cu, Ni, Co, V, Cr, U, and Th in the Niutitang Formation shale samples range 4.65437 ppm (mean Mo = 78.82 ppm), 390–40,781 ppm (mean Ba = 5064 ppm), 15.3–1386 ppm (mean Cu = 128.2 ppm), 15.1–949 ppm (mean Ni = 128.9 ppm), 0.92–22.4 ppm (mean Co = 12.72 ppm), 58.4–7585 ppm (mean V = 852.7 ppm), 59.7–871 ppm (mean Cr = 148.4 ppm), 1.97–214 ppm (mean U = 32 ppm), and 0.4–14.9 ppm (mean Th = 7.7 ppm), respectively (Table 2). Mo, Ba, Cu, Ni, Co, V, Cr, U, and Th concentrations of the Liuchapo Formation sediments vary 0.7–0.98 ppm (mean Mo = 0.84 ppm), 265–2198 ppm (mean Ba = 1232 ppm), 2.83–27 ppm (mean Cu = 14.92 ppm), 4.89–45.9 ppm (mean Ni = 25.4 ppm), 0.48–5.31 ppm (mean Co = 2.9 ppm), 12.3–134 ppm (mean V = 73.2 ppm), 108–157 ppm (mean Cr = 132.5 ppm), 0.55–5.14 ppm (mean U = 2.85 ppm), and 0.45–6.9 ppm (mean Th = 3.68 ppm), respectively.

4. Discussion

4.1. Primary Production

Zircon U–Pb geochronology has yielded an age of 536.5 ± 5.5 Ma for the Liuchapo Formation sedimentary rocks [32]. Zircon U–Pb and Re–Os geochronology has yielded ages of 521–514 Ma for the Niutitang Formation sedimentary rocks, corresponding to the Tommotian of the Early Cambrian [27,28]. The Liuchapo and Niutitang formations pre-date the radiation of vascular plants in terrestrial ecosystems, and terrigenous organic C made a negligible contribution to their TOC contents. Although sponge spicule, acanthomorphic acritarch, and scyphozoa fossils are present in the shales, biomarker analysis

of the Niutitang Formation shales indicates that planktonic algae were the main primary producers [30]. Relative to average shale [31], Niutitang Formation and Liuchapo Formation sediments have less average Al_2O_3 contents (average $Al_2O_3 = 6.99\%$), indicating minor clay minerals. Relative to average shale [31], sedimentary rocks of the Niutitang and Liuchapo formations have lower Al_2O_3 contents (average = 6.99%), indicative of the presence of only minor clay minerals. The TOC contents of mudstones or shales reflect a relatively small fraction of the primary production due to photosynthesis in the photic zone of the surface ocean [31]. Most organic material generated by primary production sinks from the ocean surface into the thermocline and deep ocean, reaches the sediment–water interface, undergoes decomposition, and is lost [33,34]. Despite this decomposition and diagenesis, TOC contents can still be used to estimate the palaeo-primary productivity [5,22].

TOC contents reach a minimum value in the upper Liuchapo Formation (ULF) and then exhibit a slightly increasing trend (Figure 3). The increasing trend of TOC contents terminates at the marlstones of the base of the Niutitang Formation (BNF), in which TOC contents decrease to 2%. The TOC contents continue to increase in the lower Niutitang Formation (LNF) and subsequently decrease in the middle Niutitang Formation (MNF). The TOC contents remain uniform at 5% until a marked decrease in the marlstones of the upper Niutitang Formation (UNF).

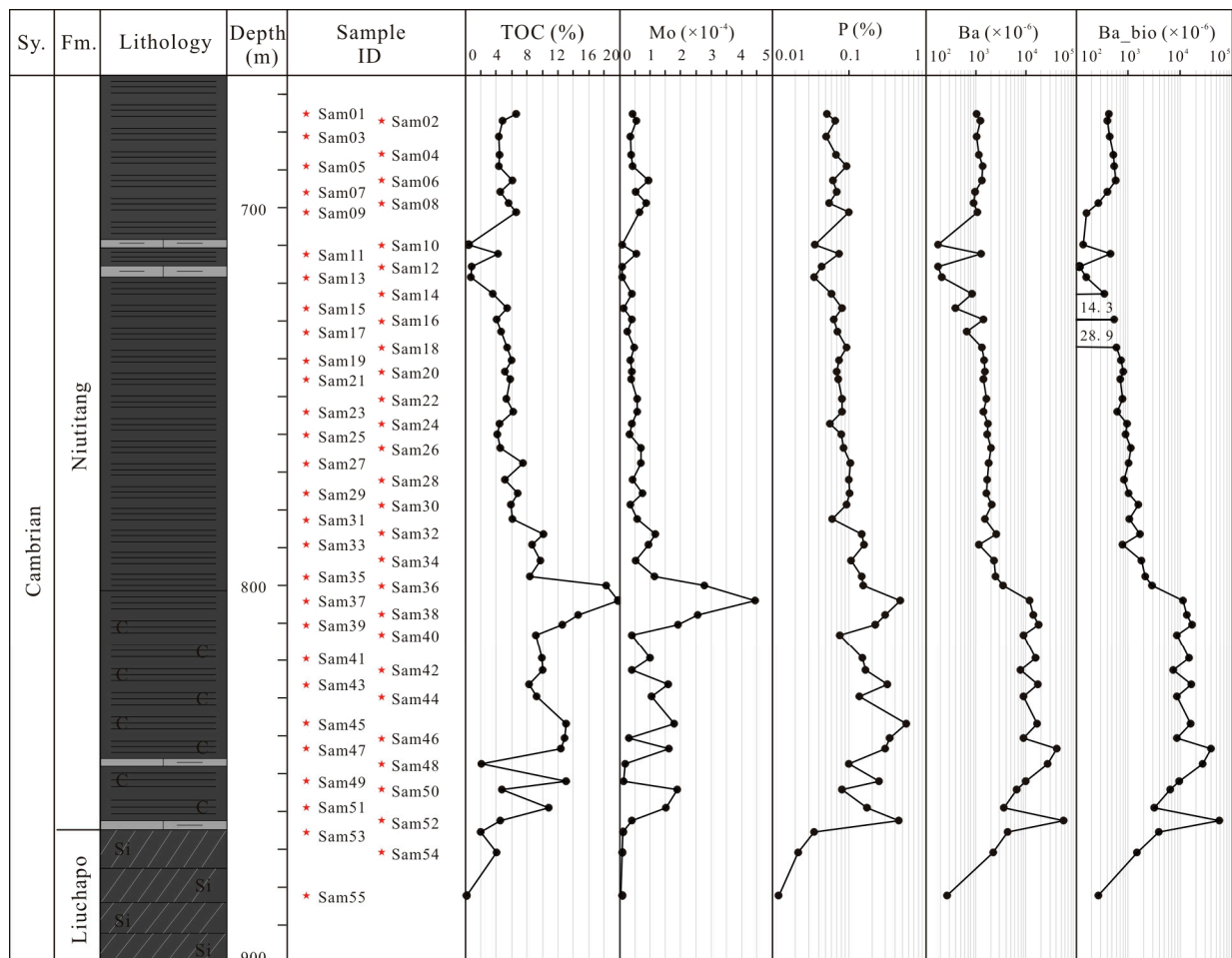


Figure 3. The primary production proxies (TOC, Mo, P, Ba, and Ba_{bio}) in the Niutitang Formation.

Molybdenum is present as MoO_4^{2-} in seawater and is rarely incorporated into natural minerals. Organic matter can scavenge Mo from the MoO_4^{2-} in seawater [35,36], or Mo can be captured as Fe–Mo–S cluster compounds that are present due to H_2S [37,38]. Owing to

the positive relationships between TOC and Mo contents, Mo provides important insights into primary productivity [39].

Molybdenum exhibits a distinctive increase at the boundary between the Liuchapo and Niutitang formations and then decreases to ~10 ppm in the marlstones in the BNF (Figure 2). Molybdenum then increases (with slight fluctuations) and peaks in the LNF. Molybdenum decreases back to ~45 ppm in the MNF. Subsequently, Mo contents remain uniform, until a distinctive decrease in the marlstones of the UNF. In general, Mo contents correlate with TOC contents throughout the Niutitang Formation (Figure 4a).

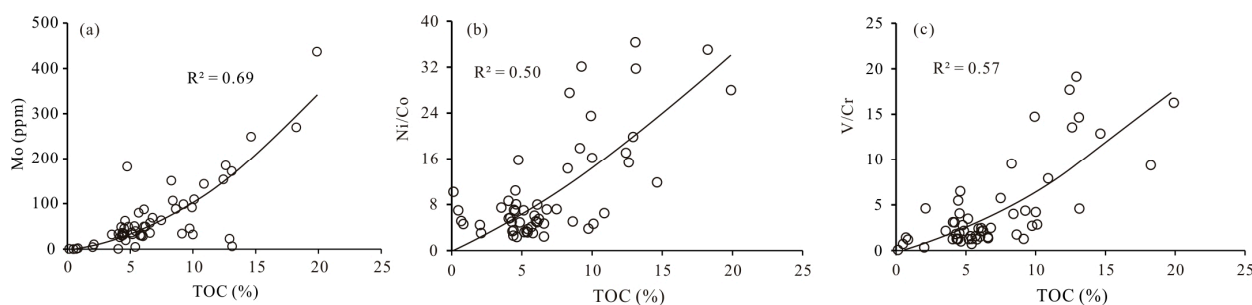


Figure 4. Crossplots of Mo, Ni/Co, and V/Cr with TOC for the Niutitang and Liuchapo Formation. (a) Mo and TOC, (b) Ni/Co and TOC, (c) V/Cr and TOC.

Phosphorus is present in dissolved and particulate form in seawater and is a prominent nutrient for microorganisms [40]. Remineralised P after burial is preferentially retained and precipitated in sediments under oxygenated bottom-water conditions but not under O₂-depleted conditions, which is attributable to differences in P fixation associated with redox cycling [41]. Although P accumulation mechanisms differ from those of TOC, P is also a proxy for primary productivity [42].

A prominent increase in P contents occurs across the boundary between the ULF and BNF, where P contents increase from 0.012 to 0.445% (Figure 2). Subsequently, P contents remain relatively high throughout the LNF, with slight fluctuations. Contents of P decrease in the overlying MNF, continue to decrease in the grey marlstones in the UNF, and then increase slightly.

Barium is derived mainly from three sources: terrigenous detrital input, hydrothermal fluids, and benthic organisms [43]. The substantial amount of Ba transported from the ocean surface zone to the sediment–water interface along with decaying organic matter is termed biogenic Ba [44]. In order to correct for the presence of detrital Ba, Dymond et al. proposed a method for determining the content of biogenic Ba (Ba_{bio}) [45]:

$$Ba_{bio} = Ba_{sample} - Al_{sample} \times (Ba/Al)_{detr}$$

where $(Ba/Al)_{detr}$ is the detrital Ba fraction estimated from the upper continental crust.

Both Ba and Ba_{bio} exhibit similar trends in the Niutitang Formation, and the contents of Ba and Ba_{bio} are almost the same (Figure 2). A prominent increase in Ba and Ba_{bio} contents occurs across the boundary between the ULF and BNF. Subsequently, Ba and Ba_{bio} contents remain relatively high throughout the LNF and then decrease. Barium and Ba_{bio} contents continue to decrease in the interval of grey marlstones in the UNF. However, the different Ba and Ba_{bio} contents in the interval of grey marlstones in the UNF may be indicative of a prominent contribution from detrital Ba.

In summary, multi-proxy data for the primary productivity in the LNF are higher than those of the overlying grey–black shales in the MNF and UNF. The primary productivity increased throughout the LNF and subsequently decreased in the MNF and UNF. In addition, the primary productivity reached a minimum during deposition of the grey marlstone intervals at the base and top of the Niutitang Formation.

4.2. Clastic Influx

Most of Ti occurs in clay minerals in sediments, and Ti normalized to Al (Ti/Al ratios) represents the detrital non-aluminosilicate input [23,46]. The Ti/Al ratios decrease to minimum values in the marlstones in the BNF. Subsequently, the Ti/Al ratios have relatively high values (with slight fluctuations) in the LNF (Figure 5), decrease slightly in the MNF, and increase in the UNF. The Ti/Al ratios return to relatively low values in the marlstone intervals of the UNF before increasing again.

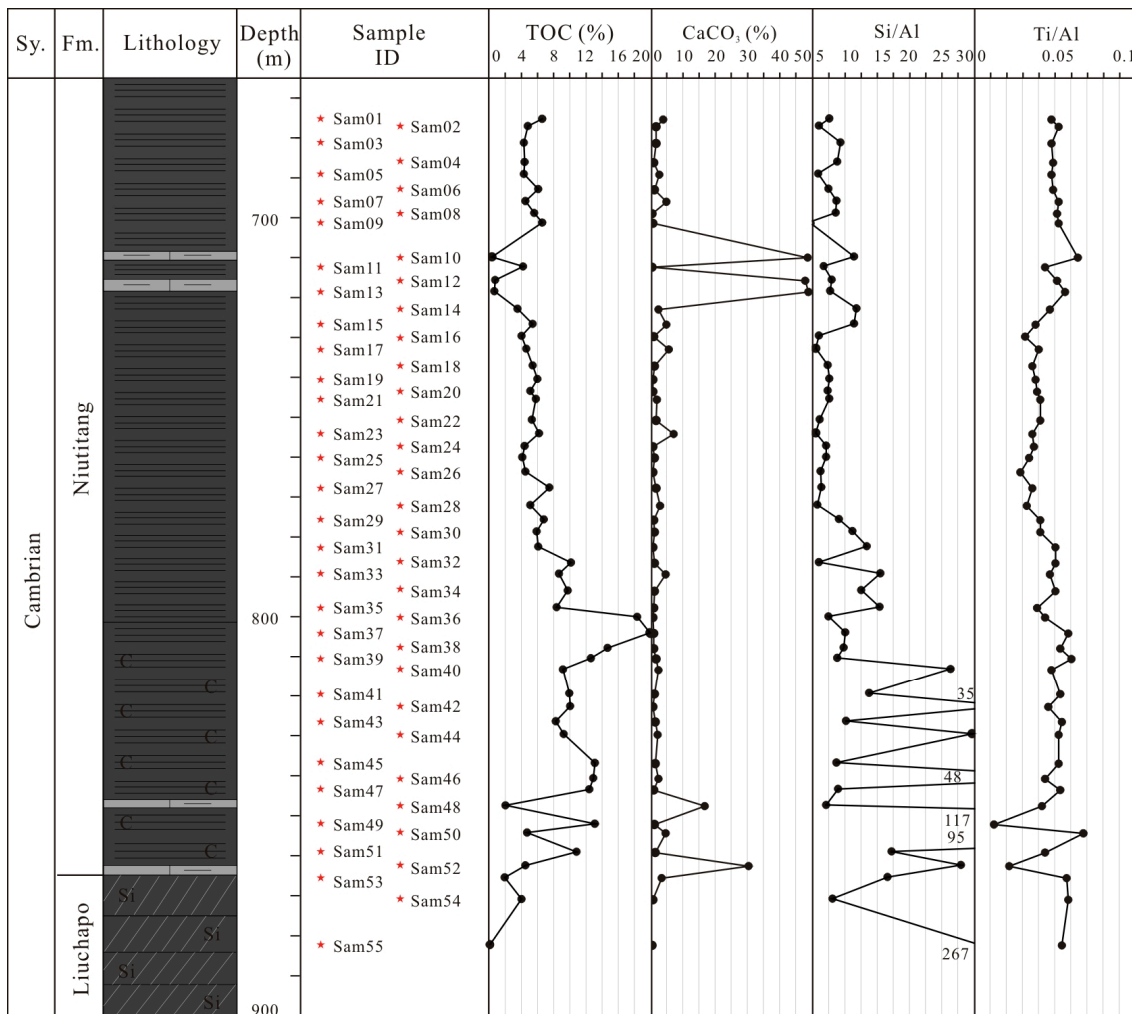


Figure 5. The dilution proxies (CaCO₃, Si/Al, and Ti/Al) in the Niutitang Formation.

The Ti/Al ratios correlate with the TOC contents, but with some notable exceptions in the marlstone intervals of the BNF and UNF, where high Ti/Al ratios correspond to low TOC contents. This might be explained by the changes in Si/Al ratios and CaCO₃ contents. The Si/Al ratios reach maximum values with prominent fluctuations in the LNF and subsequently decrease in the MNF and UNF (Figure 5). Where the Si/Al ratios begin to increase in the BNF, the Ti/Al ratios exhibit a small increase and then decrease to low ratios. The low Ti/Al ratios in the marlstone intervals of the BNF and UNF are attributable to dilution by carbonate and correspond to increases in CaCO₃ contents.

Silica is derived mainly from terrigenous detrital and biogenic silica inputs. Previous studies have proposed that excess Si contents in the BNF and LNF are attributable to the generation of biogenic silica [25]. Despite the effects of biogenic silica, the higher Si/Al ratios and minimum Ti/Al ratios in the LNF are thought to represent relatively high sea level [5]. With a rise in relative sea level, terrestrial clastic input could then weaken or cut off, resulting in the production of carbonate.

Total organic C contents increase with the sedimentation rate until a threshold value, after which the sedimentation rate dilutes the organic matter accumulation [9]. Clastic inputs increase the burial rate and prevent organic matter degradation [47] or provide more particle sites for organic matter adsorption [48]. Accordingly, Ti/Al ratios correlate well with TOC contents throughout the Niutitang Formation, apart from where dilution occurred during deposition of the marlstone intervals.

4.3. Redox Conditions

Cobalt and Cr are soluble cations in oxygenated seawater, whereas Co and Cr are transported into sediments as authigenic sulphides under anoxic conditions [49]. Because authigenic sulphides of Co and Cr are scarce, detrital/terrigenous inputs contribute most Co and Cr in sediments [28]. Vanadium and Ni are precipitated from seawater under O₂ deficient conditions, which are associated with organic matter decay [4]. Therefore, Ni/Co and V/Cr ratios are proxies of redox conditions (Figure 4b,c). Ratios of Ni/Co and V/Cr both increase (with fluctuations) across the ULP–BNF boundary and through the LNF and then decrease in the MNF and UNF (Figure 6). Relative to the MNF and UNF, the higher Ni/Co and V/Cr ratios in the LNF are indicative of an O₂-depleted depositional environment.

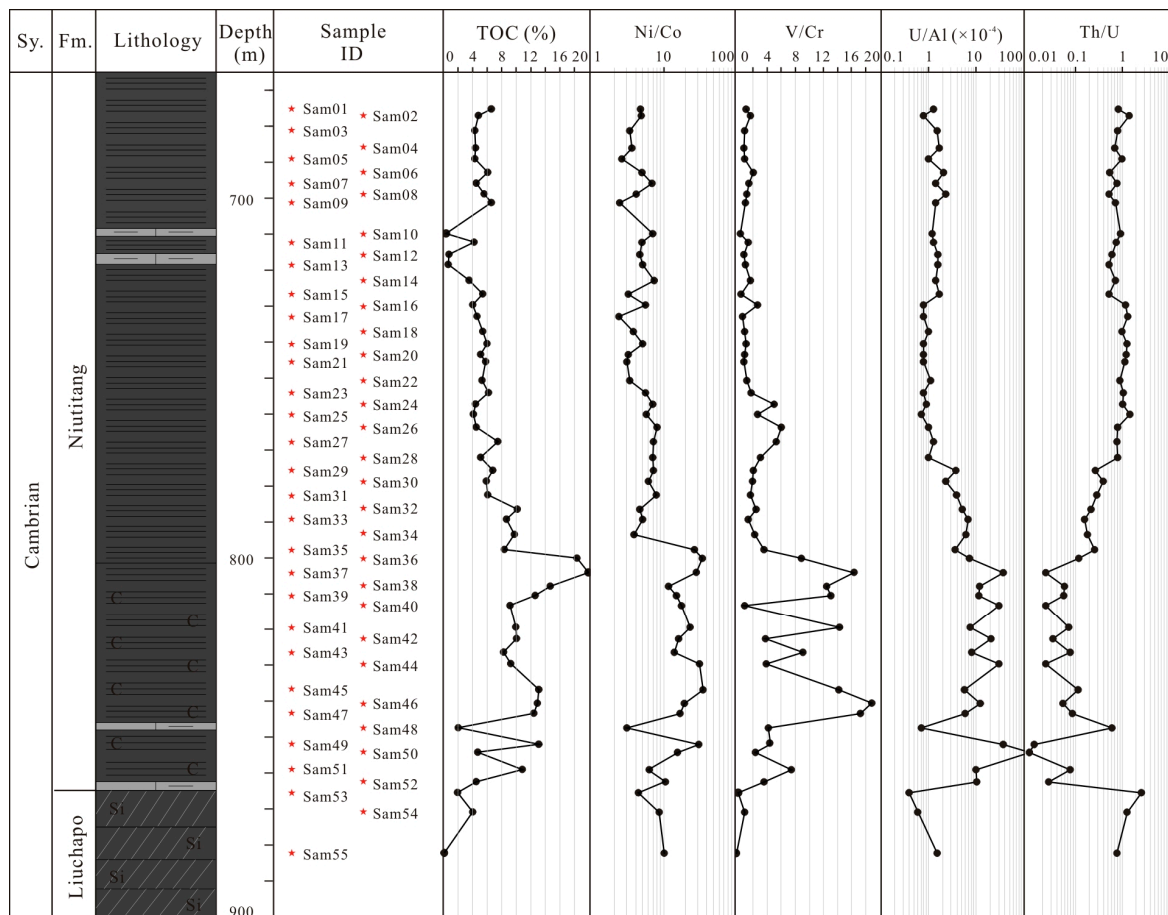


Figure 6. The redox condition proxies (Ni/Co, V/Cr, U/Al, and Th/U) in the Niutitang Formation.

Uranium occurs as dissolved U⁶⁺ in oxygenated seawater, and dissolved U⁶⁺ is reduced to insoluble U⁴⁺ under O₂-depleted conditions, resulting in U enrichment in pelagic and hemipelagic sediments [50]. Algeo and Maynard proposed that organic matter accelerated the scavenging rate of U in sediments [49]. Ratios of U/Al are 6–137 × 10⁻⁴ in the LNF and 0.7–6.9 × 10⁻⁴ in the MNF and UNF. Ratios of U/Al increase across the Liuchapo–Niutitang formation boundary and remain relatively high (with fluctuations)

throughout the LNF. Subsequently, the U/Al ratios exhibit a decrease in the MBF and UNF (Figure 6). The higher U/Al ratios of the LNF indicate the bottom waters were anoxic.

Thorium occurs as insoluble Th^{4+} in seawater and is unaffected by the redox conditions [51]. Wignall and Twitchett proposed that Th/U ratios generally increased with increasing oxygenation from 0.2 for anoxic conditions to 2–8 for oxic conditions [52]. Ratios of Th/U decrease across the Liuchapo–Niutitang formation boundary, remain relatively low with fluctuations in the LNF, and subsequently increase in the MNF and UNF (Figure 6). The lower Th/U ratios in the LNF relative to the MNF and UNF are indicative of anoxic bottom waters.

In order to discriminate euxinic from anoxic depositional conditions, Mo was used to recognise redox changes during deposition of the Niutitang Formation. Under euxinic conditions, Mo is precipitated preferentially as Fe sulphides owing to the presence of free H_2S [49]. If only U and V are scavenged and enriched without Mo, free H_2S did not exist in the seawater; however, if U, V, and Mo exhibit concurrent enrichments, then euxinic conditions existed with free H_2S [22]. Uranium, V, and Mo are all enriched in the LNF, indicating that euxinic conditions existed during deposition of the LNF.

4.4. Organic Matter Accumulation Mechanism of Organic-Rich Shales

The redox and productivity proxies suggest that the black, organic-rich shales of the LNF were deposited under anoxic (or even euxinic) conditions during periods of high primary productivity. The grey–black, organic-poor shales of the MNF and UNF were deposited under suboxic conditions during periods of relatively low primary productivity.

Euhedral pyrite is either precipitated directly or formed indirectly by framboidal precursor regrowth, indicative of limited FeS_2 saturation and intense late diagenesis [53]. Framboidal pyrite in marine sediments has two main mechanisms of formation: (1) under oxic–dysoxic bottom-water conditions, in which diagenetic, framboidal pyrite grows in anoxic pore waters in sediments [54]; and (2) under euxinic bottom-water conditions, in which syngenetic framboidal pyrite grows in anoxic bottom waters and sinks into the sediments [55]. Framboidal pyrite dominates over euhedral pyrite in the Niutitang Formation sediments (Figure 7), indicating the framboidal pyrite could be an indicator of the redox environment. The mean diameter and size distribution of framboidal pyrite in the Niutitang Formation sediments suggest the pyrite formed under euxinic conditions [55]. Based on organic biomarker analysis, the main primary producers were planktonic algae [35]. Planktonic algae might have produced mineralised tests that sank into the sediments.

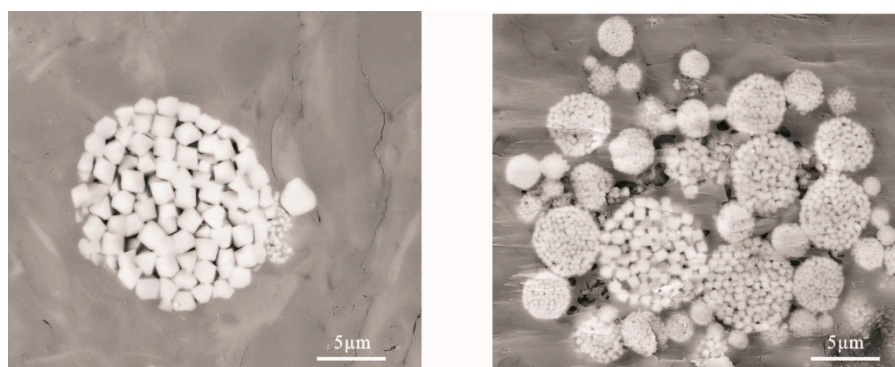


Figure 7. Pyrite in the organic-rich Niutitang Formation.

Owing to tectonic subsidence in the Huanan rift and a relative rise in sea level [22], the accommodation space increased during deposition of the LNF. Because of the rapid transgression at the Ediacaran–Cambrian boundary, the Niutitang Formation is divided into transgressive and highstand systems tracts [21]. During deposition of the LNF, the relative sea level rose to the maximum flooding surface and the seasonal mixing could not affect the bottom waters [25,26]. Biomarker analyses show that nutrients were derived from planktonic algae [30], and upwelling provided nutrients for primary producers based

on the occurrence of phosphorites and P enrichment. Productivity proxies (Mo and Ba_{bio}) show that primary productivity was higher in the ocean surface zone during deposition of the LNF shales. The high primary productivity enhanced the organic C flux into the chemocline layer and bottom waters, leading to the development of anoxic bottom waters owing to O_2 consumption by microorganisms and organic matter degradation. In addition, clastic inputs increased the burial rate and prevented organic matter degradation. The anoxic bottom waters were beneficial for the preservation of organic matter in the LNF shales (Figure 8).

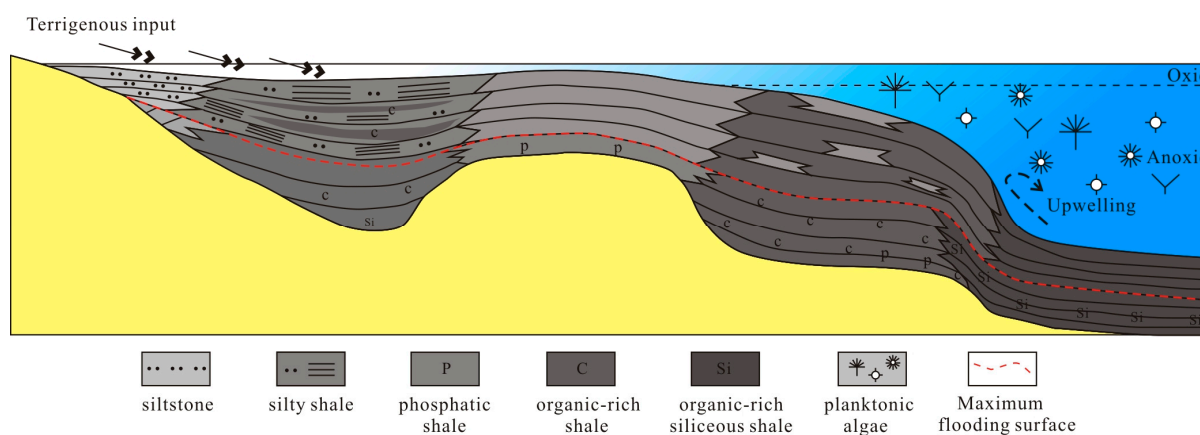


Figure 8. Conceptual model showing the organic matter enrichment mechanisms of the Niutitang Formation shales.

During deposition of the grey–black MNF and UNF shales, relative sea level fell and primary productivity decreased. Seasonal mixing may have reached the bottom waters and, in addition, low primary productivity would not have formed anoxic bottom waters. The low primary productivity and suboxic bottom waters would have resulted in the relatively organic-poor MNF and UNF shales.

5. Conclusions

1. Redox and primary productivity proxies suggest that the black, organic-rich shales in the Niutitang Formation were deposited in anoxic–euxinic conditions during periods of high primary productivity;
2. Framboidal pyrite indicates that anoxic bottom waters existed during organic matter deposition. The high primary productivity enhanced the organic C flux into the thermocline layer and bottom waters, which formed the O_2 -depleted bottom waters;
3. Ti/Al ratios correlate with TOC contents throughout the Niutitang Formation, indicating the clastic input enhanced the burial rate and prevented organic matter degradation during deposition of the Niutitang Formation.

Author Contributions: Conceptualization, L.Z. (Lei Zhou); methodology, L.Z. (Linyan Zhang); software, L.Z. (Linyan Zhang); validation, L.W.; formal analysis, L.Z. (Linyan Zhang); investigation, L.Z. (Lei Zhou); resources, X.F. and L.W.; data curation, L.Z. (Linyan Zhang); writing—original draft, L.Z. (Lei Zhou); writing—review and editing, L.Z. (Lei Zhou); visualization, L.W.; supervision, X.F.; project administration, X.F.; funding acquisition, X.F. All authors have read and agreed to the published version of the manuscript.

Funding: This research was funded by the National Natural Science Foundation of China (42372179), the China Postdoctoral Science Foundation (2018M631541), and the China Geological Survey (DD20221660).

Data Availability Statement: Data are contained within the article.

Acknowledgments: We thank the Institute of Geomechanics, Chinese Academy of Geological Sciences for the provision of geological data and borehole samples. The careful review and constructive suggestions of the manuscript by anonymous reviewers are greatly appreciated.

Conflicts of Interest: The authors declare no conflict of interest.

References

1. Bohacs, K.M.; Grawbowski, G.J.; Carroll, A.R.; Mankeiwitz, P.J.; Miskell-Gerhardt, K.J.; Schwalbach, J.R.; Wegner, M.B.; Simo, J.A. Production, and dilution—The many paths to source-rock development. In *Deposition of Organic-Carbon-rich Sediments: Models, Mechanisms and Consequences*; SEPM Special Publication: Tulsa, OK, USA, 2005; pp. 61–101.
2. Passey, Q.R.; Bohacs, K.M.; Esch, W.L.; Klimentidis, R.; Sinha, S. From oil-prone source rock to gas-producing shale reservoir-geologic and petrophysical characterization of unconventional shale gas reservoirs. In Proceedings of the SPE 131350, SPE International Oil & Gas Conference and Exhibition, Beijing, China, 8–10 June 2010.
3. Wang, Z.W.; Wang, J.; Fu, X.G.; Zhan, W.Z.; Yu, F.; Feng, X.L.; Song, C.Y.; Chen, W.B.; Zeng, S.Q. Organic material accumulation of Carnian mudstones in the North Qiangtang Depression, eastern Tethys: Controlled by the paleoclimate, paleo-environment, and provenance. *Mar. Petrol. Geol.* **2017**, *88*, 440–457. [\[CrossRef\]](#)
4. Calvert, S.E.; Pedersen, T.F. Geochemistry of recent oxic and anoxic marine sediments: Implications for the geological record. *Mar. Geol.* **1993**, *113*, 67–88. [\[CrossRef\]](#)
5. Sageman, B.B.; Murphy, A.E.; Werne, J.P.; Ver Straeten, C.A.; Hollander, D.J.; Lyons, T.W. A tale of shales: The relative roles of production, decomposition, and dilution in the accumulation of organic-rich strata, Middle–Upper Devonian, Appalachian basin. *Chem. Geol.* **2003**, *195*, 229–273. [\[CrossRef\]](#)
6. Wei, H.Y.; Chen, D.Z.; Wang, J.G.; Yu, H.; Tucker, M.E. Organic accumulation in the lower Chihhsia Formation (Middle Permian) of South China: Constraints from pyrite morphology and multiple geochemical proxies. *Paleogeogr. Palaeoclimatol.* **2012**, *353–355*, 73–86. [\[CrossRef\]](#)
7. Algeo, T.J.; Henderson, C.M.; Tong, J.N.; Feng, Q.L.; Yin, H.F.; Tyson, R.V. Plankton and productivity during the Permian–Triassic boundary crisis: An analysis of organic carbon fluxes. *Glob. Planet. Chang.* **2013**, *105*, 52–67. [\[CrossRef\]](#)
8. Creaney, S.; Passey, Q.R. Recurring patterns of total organic carbon and source rock quality within a sequence stratigraphic framework. *AAPG Bull.* **1993**, *77*, 386–401.
9. Tyson, R.V. Sedimentation rate, dilution, preservation and total organic carbon: Some results of a modelling study. *Org. Geochem.* **2001**, *32*, 333–339. [\[CrossRef\]](#)
10. Henrichs, S.M.; Reeburgh, W.S. Anaerobic mineralization of marine sediment organic matter: Rates and the role of anaerobic processes in the oceanic carbon economy. *Geomicrobiol. J.* **1987**, *5*, 191–238. [\[CrossRef\]](#)
11. Demaison, G.J.; Moore, G.T. Anoxic environments and oil source bed genesis. *Org. Geochem.* **1980**, *2*, 9–31. [\[CrossRef\]](#)
12. Calvert, S.E.; Bustin, R.M.; Ingall, E.D. Influence of water column anoxia and sediment supply on the burial and preservation of organic carbon in marine shales. *Geochim. Cosmochim. Acta* **1996**, *60*, 1577–1593. [\[CrossRef\]](#)
13. Yan, D.T.; Wang, H.; Fu, Q.L.; Chen, Z.H.; He, J.; Gao, Z. Geochemical characteristics in the Longmaxi Formation (Early Silurian) of South China: Implications for organic matter accumulation. *Mar. Petrol. Geol.* **2015**, *65*, 290–301. [\[CrossRef\]](#)
14. Peng, J. What besides redox conditions? Impact of sea-level fluctuations on redox-sensitive trace-element enrichment patterns in marine sediments. *Sci. China Earth Sci.* **2022**, *65*, 1985–2004. [\[CrossRef\]](#)
15. Peng, J.W.; Larson, T. A novel integrated approach for chemofacies characterization of organic-rich mudrocks. *AAPG Bull.* **2022**, *106*, 437–460. [\[CrossRef\]](#)
16. Liang, C.; Jiang, Z.X.; Guo, L.; Yang, Y.T. Characteristics of black shale, sedimentary evolution and shale gas exploration prospect of shelf face taking Wengan and Yongye profile of the Niutitang Formation as an example. *J. Daqing Petrol. Inst.* **2011**, *35*, 13–21.
17. Mei, M.X.; Zhang, H.; Meng, X.Q.; Chen, Y.H. Sequence stratigraphic division and framework of the Lower Cambrian in the Upper Yangtze region. *Geol. China* **2006**, *33*, 1292–1304.
18. Wu, Y.; Fan, T.L.; Jiang, S.; Yang, X.Q. Lithofacies and sedimentary sequence of the lower Cambrian Niutitang shale in the upper Yangtze platform, South China. *J. Nat. Gas Sci. Eng.* **2017**, *43*, 124–136. [\[CrossRef\]](#)
19. Wu, Y.; Fan, T.L.; Ding, H.Y. Lithofacies and Sedimentary Model of the Lower Cambrian Marine Shale in the Upper Yangtze Platform. *Geoscience* **2017**, *31*, 1222–1232.
20. Arthur, M.A.; Sageman, B.B. Marine black shales: Depositional mechanisms and environments of ancient deposits. *Annu. Rev. Earth Planet Sci.* **1994**, *22*, 499–551. [\[CrossRef\]](#)
21. Jones, B.; Manning, D.A.C. Comparison of geochemical indices used for the interpretation of palaeoredox conditions in ancient mudstones. *Chem. Geol.* **1994**, *111*, 111–129. [\[CrossRef\]](#)
22. Tribouillard, N.; Algeo, T.J.; Lyons, T.; Riboulleau, A. Trace metals as paleoredox and paleoproductivity proxies: An update. *Chem. Geol.* **2006**, *232*, 12–32. [\[CrossRef\]](#)
23. Ross, D.J.K.; Bustin, R.M. Investigating the use of sedimentary geochemical proxies for paleoenvironment interpretation of thermally mature organic-rich strata: Examples from the Devonian–Mississippian shales, Western Canadian Sedimentary Basin. *Chem. Geol.* **2009**, *200*, 1–19. [\[CrossRef\]](#)

24. Shields, G.; Stille, P. Diagenetic constraints on the use of cerium anomalies as palaeoseawater redox proxies: An isotopic and REE study of Cambrian phosphorites. *Chem. Geol.* **2001**, *175*, 29–48. [[CrossRef](#)]
25. Li, Y.F.; Fan, T.L.; Zhang, J.C.; Zhang, J.P.; Wei, X.J.; Hu, X.L.; Zeng, W.T.; Fu, W. Geochemical changes in the Early Cambrian interval of the Yangtze Platform, South China: Implications for hydrothermal influences and paleocean redox conditions. *J. Asian Earth Sci.* **2015**, *109*, 100–123. [[CrossRef](#)]
26. Zhou, L.; Kang, Z.H.; Wang, Z.X.; Peng, Y.Y.; Xiao, H.F. Sedimentary geochemical investigation for paleoenvironment of the Lower Cambrian Niutitang Formation shales in the Yangtze Platform. *J. Petrol. Sci. Eng.* **2017**, *159*, 376–386. [[CrossRef](#)]
27. Mao, J.W.; Lehmann, B.; Du, A.D.; Zhang, G.D.; Ma, D.S.; Wang, Y.T.; Zeng, M.G.; Kerrich, R. Re-Os dating of polymetallic Ni-Mo-PGE-Au mineralization in Lower Cambrian black shales of South China and its geologic significance. *Econ. Geol.* **2002**, *97*, 1051–1061. [[CrossRef](#)]
28. Jiang, S.Y.; Yang, J.H.; Ling, H.F.; Chen, Y.Q. Extreme enrichment of polymetallic Ni–Mo–PGE–Au in lower Cambrian black shales of South China: An Os isotope and PGE geochemical investigation. *Paleogeogr. Paleocl.* **2007**, *254*, 217–228. [[CrossRef](#)]
29. Xu, L.G.; Lehmann, B.; Mao, J.W. Seawater contribution to polymetallic Ni–Mo–PGE–Au mineralization in Early Cambrian black shales of South China: Evidence from Mo isotope, PGE, trace element, and REE geochemistry. *Ore Geol. Rev.* **2013**, *52*, 66–84. [[CrossRef](#)]
30. Liu, Z.H.; Zhuang, X.G.; Teng, G.E.; Xie, X.M.; Yin, L.M.; Bian, L.Z.; Feng, Q.L.; Algeo, T.J. The Lower Cambrian Niutitang Formation at Yangtiao (Guizhou, SW China): Organic matter enrichment, source rock potential, and hydrothermal influences. *J. Petrol. Geol.* **2015**, *38*, 411–432. [[CrossRef](#)]
31. Wedepohl, K.H. Environmental influences on the chemical composition of shales and clays. In *Physics and Chemistry of the Earth*; Ahrens, L.H., Press, F., Runcorn, S.K., Urey, H.C., Eds.; Pergamon: Oxford, UK, 1971; Volume 8, pp. 307–331.
32. Chen, D.; Wang, J.; Qing, H.; Yan, D.; Li, R. Hydrothermal venting activities in the Early Cambrian, south China: Petrological, geochronological and stable isotopic constraints. *Chem. Geol.* **2009**, *258*, 168–181. [[CrossRef](#)]
33. Schoepfer, S.D.; Shen, J.; Wei, H.Y.; Tyson, R.V.; Ingall, E.; Algeo, T.J. Total organic carbon, organic phosphorus, and biogenic barium fluxes as proxies for paleomarine productivity. *Earth-Sci. Rev.* **2014**, *149*, 23–52. [[CrossRef](#)]
34. Hedges, J.I.; Keil, R.G. Sedimentary organic matter preservation: An assessment and speculative synthesis. *Mar. Chem.* **1995**, *49*, 81–115. [[CrossRef](#)]
35. Helz, G.R.; Miller, C.V.; Charnock, J.M.; Mosselmans, J.L.W.; Patrick, R.A.D.; Garner, C.D.; Vaughan, D.J. Mechanisms of molybdenum removal from the sea and its concentration in black shales: EXAFS evidences. *Geochim. Cosmochim. Acta* **1996**, *60*, 3631–3642. [[CrossRef](#)]
36. Adelson, J.M.; Helz, G.R.; Miller, C.V. Reconstructing the rise of recent coastal anoxia; molybdenum in Chesapeake Bay sediments. *Geochim. Cosmochim. Acta* **2001**, *65*, 237–252. [[CrossRef](#)]
37. Bertine, K.K. The deposition of molybdenum in anoxic waters. *Mar. Chem.* **1972**, *1*, 43–53. [[CrossRef](#)]
38. Ripley, E.M.; Shaffer, N.R.; Gilstrap, M.S. Distribution and geochemical characteristics of metal enrichment in the New Albany Shale (Devonian–Mississippian), Indiana. *Econ. Geol.* **1990**, *85*, 1790–1807. [[CrossRef](#)]
39. Werne, J.P.; Sageman, B.B.; Lyons, T.W.; Hollander, D.J. An integrated assessment of a “type euxinic” deposit: Evidence for multiple controls on black shale deposition in the Middle Devonian Oatka Creek Formation. *Am. J. Sci.* **2002**, *302*, 110–143. [[CrossRef](#)]
40. Paytan, A.; McLaughlin, K. The oceanic phosphorus cycle. *Chem. Rev.* **2007**, *107*, 563–576. [[CrossRef](#)] [[PubMed](#)]
41. Ingall, E.D.; Kolowith, L.; Lyons, T.; Hurtgen, M. Sediment carbon, nitrogen and phosphorus cycling in an anoxic fjord, Effingham Inlet, British Columbia. *Am. J. Sci.* **2005**, *305*, 240–258. [[CrossRef](#)]
42. Ingall, E.R.; Bustin, M.; Cappellen, P.V. Influence of water column anoxia on the burial and preservation of carbon and phosphorus in marine shales. *Geochim. Cosmochim. Acta* **1993**, *57*, 303–316. [[CrossRef](#)]
43. Bertram, M.A.; Cowen, J.P. Morphological and compositional evidence for biotic precipitation of marine barite. *J. Mar. Res.* **1997**, *55*, 577–593. [[CrossRef](#)]
44. Ganeshram, R.S.; François, R.; Commeau, J.; Brown-Leger, S.L. An experimental investigation of barite formation in seawater. *Geochim. Cosmochim. Acta* **2003**, *67*, 2599–2605. [[CrossRef](#)]
45. Dymond, J.; Suess, E.; Lyle, M. Barium in deep-sea sediment: A geochemical proxy for paleoproductivity. *Paleoceanography* **1992**, *7*, 163–181. [[CrossRef](#)]
46. Bertrand, P.; Shimmield, G.; Martinez, P.; Grousset, F.; Jorissen, F.; Paterne, M.; Pujol, C.; Bouloubassi, I.; Buat Menard, P.; Peypouquet, J.P.; et al. The glacial ocean productivity hypothesis: The importance of regional temporal and spatial studies. *Mar. Geol.* **1996**, *130*, 1–9. [[CrossRef](#)]
47. Ibach, L.E.J. Relationship between sedimentation rate and total organic carbon content in ancient marine sediments. *AAPG Bull.* **1982**, *66*, 170–188.
48. Zeng, S.Q.; Wang, J.; Fu, X.G.; Chen, W.B.; Feng, X.L.; Wang, D.; Song, C.Y.; Wang, Z.W. Geochemical characteristics, redox conditions, and organic matter accumulation of marine oil shale from the Changliang Mountain area, northern Tibet, China. *Mar. Petrol. Geol.* **2015**, *64*, 203–221. [[CrossRef](#)]
49. Algeo, T.J.; Maynard, J.B. Trace-element behavior and redox facies in core shales of Upper Pennsylvanian Kansas-type cyclothems. *Chem. Geol.* **2004**, *206*, 289–318. [[CrossRef](#)]

50. McManus, J.; Berelson, W.M.; Klinkhammer, G.P.; Hammond, D.E.; Holm, C. Authigenic uranium: Relationship to oxygen penetration depth and organic carbon rain. *Geochim. Cosmochim. Acta* **2005**, *69*, 95–108. [[CrossRef](#)]
51. Kimura, H.; Watanabe, Y. Oceanic anoxia at the Precambrian-Cambrian boundary. *Geology* **2001**, *29*, 995–998. [[CrossRef](#)]
52. Wignall, P.B.; Twitchett, R.J. Oceanic anoxia and the end Permian mass extinction. *Science* **1996**, *272*, 1155–1158. [[CrossRef](#)]
53. Khan, D.; Qiu, L.W.; Liang, C.; Mirza, K.; Rehman, S.U.; Han, Y.; Hannan, A.; Kashif, M.; Kra, K.L. Genesis and distribution of pyrite in the lacustrine shale: Evidence from the Es3x shale of the Eocene Shahejie Formation, Zhanhua Sag, East China. *ACS Omega* **2022**, *7*, 1244–1258. [[CrossRef](#)]
54. Zhao, J.; Liang, J.L.; Long, X.P.; Li, J.; Xiang, Q.R.; Zhang, J.C.; Hao, J.L. Genesis and evolution of framboidal pyrite and its implications for the oreforming process of Carlin-style gold deposits, southwestern China. *Ore Geol. Rev.* **2018**, *102*, 426–436. [[CrossRef](#)]
55. Chang, J.Y.; Li, Y.Y.; Lu, H.L. The morphological characteristics of authigenic pyrite formed in marine sediments. *J. Mar. Sci. Eng.* **2022**, *10*, 1533. [[CrossRef](#)]

Disclaimer/Publisher’s Note: The statements, opinions and data contained in all publications are solely those of the individual author(s) and contributor(s) and not of MDPI and/or the editor(s). MDPI and/or the editor(s) disclaim responsibility for any injury to people or property resulting from any ideas, methods, instructions or products referred to in the content.